https://doi.org/10.5194/nhess-2024-150
Preprint. Discussion started: 22 August 2024

Natural Hazards and Earth System Sciences
Discussions

Dynamic Fragility of a Slender Rock Pillar in a Sedimentary Rock Mass – from rock mechanics to seismic hazard

Alaa Jbara[1], Michael Tsesarsky[1,2]

[1] Department of Civil and Environmental Engineering, Ben Gurion University of the Negev, Beer-Sheva 84105, Israel
[2] Department of Earth and Environmental Sciences, Ben Gurion University of the Negev, Beer-Sheva 84105, Israel

Correspondence to: Michael Tsesarsky (michatse@bgu.ac.il)

Abstract. Fragile geological features (FGF) are the only empirical data to validate seismic hazard analysis over prehistoric timescales. Precariously balanced rocks (PBR) are the most common FGF in practice, with fragility analysis based on rigid body rocking dynamics. FGFs evolved from sedimentary rock masses cannot be treated as rigid blocks, and rock mass properties should be considered in their fragility analysis. Contrary to PBRs, sedimentary FGFs received limited attention from the geological and engineering communities. This paper presents a comprehensive dynamic fragility analysis of a 42-meter-high pillar - the Ramon Pillar (Negev Desert, Israel). The pillar is comprised of a sedimentary rock mass with various discontinuities. An accurate finite elements (FE) model of the pillar ($1.25 \cdot 10^6$ elements) was developed based on high-resolution aerial LiDAR scanning and in-situ measurements of rock elastic modulus along its entire height. The model was validated by comparing computational modal analysis with in-situ measurements of natural vibrations. The first mode of 1.3 Hz was precisely predicted. The second mode was predicted with a 10% difference: 2.7 Hz calculated compared to 3 Hz measured. An a-priory assumption of rock elastic modulus (or back-calculation) or simplified geometries yielded unsatisfactory results. Following the successful validation, a fully dynamic fragility analysis of the pillar was performed, using recorded ground motions, to study the basal tensile stresses. Located in a region with two seismic sources, the Sinai Negev Shear Zone (SNSZ) and the Dead Sea Transform (DST), the pillar's fragility analysis was used to test regional seismic hazard estimates. It was found that an M 6 earthquake on the SNSZ will probably lead to breakage of the pillar at its base due to stresses exceeding its basal strength. Given a fragility age of 11.4 ky, our analysis challenges the assumption that the SNSZ can produce an M 6 event.

1 Introduction

The recurrence intervals of large earthquakes generally exceed the observation length of instrumental records; hence, existing catalogs cannot provide complete information on seismic sources and seismic hazards (Anderson et al., 2011). Whereas historical records are useful in constraining the return periods, they are less useful in constraining earthquake locations, magnitudes, and ground motion intensity. The standard method used to assess the hazard of potentially damaging earthquakes is the probabilistic seismic hazard analysis (PSHA). This framework allows for estimating the rate or probability of exceeding

https://doi.org/10.5194/nhess-2024-150
Preprint. Discussion started: 22 August 2024


Natural Hazards and Earth System Sciences
Discussions

ground-motion intensity at a site (Gerstenberger et al., 2020). Whereas the underlying assumptions of PSHA are still debated (e.g., Mulargia et al., 2017;Stark, 2022;Bommer, 2022) its widespread use in the earthquake engineering community requires independent validation (Marzocchi and Meletti, 2024).

Geologic constraints are the only empirical data to validate PSHA estimates over prehistoric timescales. The development of robust and quantitative validation and evaluation methods to reduce uncertainties in earthquake ground-motion estimates are particularly required at long return periods (10^3 to 10^4 yr) because PSHA estimates for such return periods are highly uncertain yet essential for the siting, design, and continued maintenance and monitoring of critical civic facilities, such as large dams, power plants (including nuclear), and nuclear waste repositories (Rood et al., 2020). Ancient, fragile geologic features (FGF) have been previously identified as potentially useful for validating un-exceeded ground motions estimated from PSHA models (Anderson et al., 2011 and references therein;Stirling and Anooshehpoor, 2006), and were recently incorporated into formal design earthquake motions for a significant engineered structure (Stirling et al., 2021).

1.1 Fragile Geological Features

A fragile geological feature (FGF) is a feature that might be easily destroyed by strong earthquake ground motions and is mechanically simple enough to analyze the ground motions that might cause its destruction (Anderson et al., 2011). FGFs include various delicate natural features such as paleo-sea stacks, tufa towers, hoodoos, badlands, and unstable regoliths, which can potentially be used to constrain past ground motions (Stirling et al., 2020). In practice, the most common FGF is the precariously balanced rocks (PBR), introduced by Brune (1996) for PSHA applications in Southern California and Nevada. PBRs are boulders balanced on and mechanically separated from a sub-horizontal pedestal and are susceptible to topple when exposed to earthquake ground shaking.

The ubiquity of granitic PBRs near the San Andreas fault system enabled statistically meaningful analysis and reduced uncertainties in earthquake hazard analysis (Rood et al., 2020). The relative simplicity in determining the fragility of PBRs enabled the spread of the method worldwide. However, this method cannot be readily exported to different geological terrains (i.e., non-granitic) as the mechanical response to dynamic loading of various FGFs fundamentally differs from the rocking dynamics of PBRs. In a recent workshop on "*Evaluation of seismic hazard models with fragile geological features*" (Stirling et al., 2021) ,the topic of "*fragility estimation*" was recognized as a critical research need. Specifically, with emphasis on "*Case studies of the fragility of various categories of FGF*s" and "*cost- and time-effective methods for quantifying fragility that accounts for frequency content of ground motions*", that will yield "*greater confidence in fragility assessment*" and "*greater uptake of FGF data for constraining seismic hazard models*".

1.2 Dynamic analysis of FGFs

Contrary to granitic PBRs, FGFs evolving from sedimentary rock masses, such as rock pillars and towers, received limited attention from the geological and engineering communities. For sedimentary FGFs, partial basal attachment along bedding planes should be assumed. Shang et al. (2018) showed that in siltstone, an incipient bedding plane's uniaxial tensile strength (UTS) ranged from 32% to 88% of the parent rock UTS. Rock joints in the same rock type exhibited UTS of 23% to 70% of

https://doi.org/10.5194/nhess-2024-150
Preprint. Discussion started: 22 August 2024


Natural Hazards and Earth System Sciences Discussions

parent rock, and rock bridges consisted of 23% to 70% of the discontinuity. Frayssines and Hantz (2009) showed that steep limestone cliffs were stable due to relatively small rock bridges, up to 5% of the failure surface. Any attempt to quantify rock bridges is exacerbated by the fact that rock bridges are not visible unless human activities or natural events expose the rock mass (Elmo et al., 2018). Should rock bridges be neglected in hazard assessment, the analysis would conclude that cliffs that existed from the centennial to millennial time scales have low safety factors. Therefore, realistic hazard assessment must consider the rock bridges on potential failure surfaces.

Accurate estimation of natural frequencies, elastic moduli, and damping ratios is critical for assessing the dynamic fragility of freestanding rock structures. Several research groups studied the vibrational behavior of freestanding rock masses, such as rock arches (Moore et al., 2018;Moore et al., 2016) and rock towers (Moore et al., 2019;Valentin et al., 2017). Combined with numerical analysis to back-calculate the elastic (small strain) moduli, the seismic resonance technique proved feasible to determine the natural modes and the elastic moduli of freestanding rock masses. Specifically, Moore et al. (2019) claim that with basic geometry and material properties estimates, other freestanding rock structures' resonant frequencies can be estimated a priori. It should be noted that installing seismometers atop large-scale structures, such as the 120 m high Castleton tower in Utah (Moore et al., 2019), is not a simple task involving rock climbing and rappelling expertise.

In what follows, we present a comprehensive analysis of the dynamic fragility of a slender rock pillar (Ramon, Israel) based on accurate LiDAR scanning of its geometry, in-situ rock elastic modulus determination, and FEM modal and dynamic analysis. We validate the mechanical model by comparing the results of the modal analysis to vibrational measurements of the pillar (Finzi et al., 2020). The validated model was then used for a dynamic FE analysis for various loading (distance – magnitude) scenarios. The dynamic analysis results are used to challenge previous assumptions regarding the region's seismic hazard.

2 Negev Desert Seismic Hazard

The seismic hazard of the central Negev (Israel) is dominated by two seismogenic sources: the Sinai-Negev Shear Zone (SNSZ) and the Dead Sea Transform (DST). The SNSZ includes five E–W trending faults (Fig. 1), from north to south: Saad–Nafha, Ramon, Arif–Batur, Paran, and Thamad. The region exhibits low modern-day seismicity. Seismic hazard studies regard the entire zone cautiously by setting a relatively high maximal magnitude of M 6.2 (Grünthal et al., 2009); other studies (Shamir et al., 2001) and the Israeli earthquake building code consider only the Thamad and Paran faults as seismic sources, capable of producing M 6 earthquakes.

The active tectonic border Dead Sea Transform (DST) is the second regional seismogenic source. The DST, with a total length of 1100 km, consists of several en-echelon segments and large pull-apart basins such as the Dead Sea and the Gulf of Aqaba (Garfunkel, 2014). The Arava Valley is located between these basins, accommodating a relatively simple linear segment of the DST, the Arava fault, characterized by almost pure strike-slip motion with a slip rate of about 4-5 mm/year (Hamiel et al., 2016). While the DST (at large) has been responsible for numerous $M \geq 7$ earthquakes in the last 3000 years (Agnon,

https://doi.org/10.5194/nhess-2024-150
Preprint. Discussion started: 22 August 2024

Natural Hazards and Earth System Sciences
Discussions

95 2014;Zohar, 2019), only a few significant events were documented along the Arava fault section (Lefevre et al., 2018). There is a wide range of uncertainty regarding the magnitudes of earthquakes along this remote section. The challenge in deciphering historical data is demonstrated in the case of the 873 CE event, which some studies suggest to be the strongest historical earthquake in the region, M 7 to 7.5 (Lefevre et al., 2018;Klinger et al., 2015), while other studies do not mention it at all (Ambraseys et al., 2005).

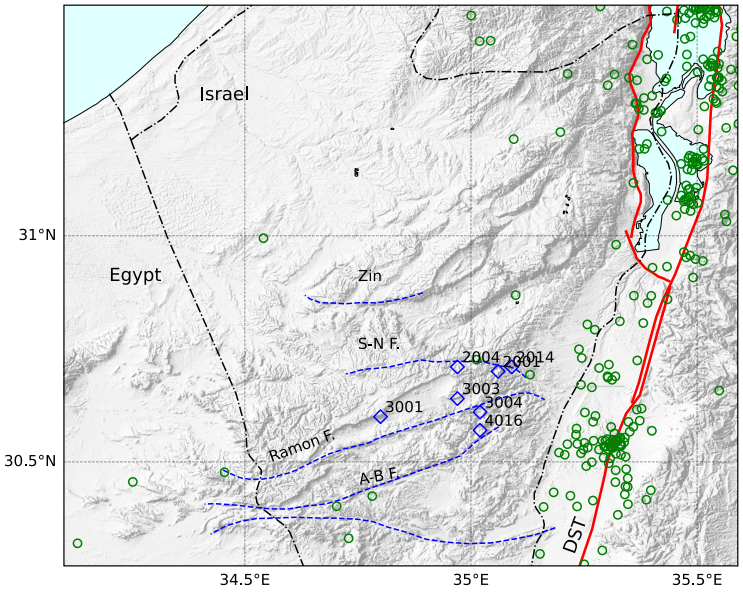

100

Figure 1: .Regional shaded relief map of Southern Israel. Dead Sea Transform (DST) active faults are plotted with continuous red lines, and the Sinai Negev Shear Zone faults are plotted with broken blue lines. S-N F. is Sa'ad-Nafha Fault, A-B F. is Arif-Bator fault. Blue diamonds are the locations of dated rock pillars (Finzi et al., 2020). Green circles are seismic events (Israel Seismic Catalog, 2013 - 2023, M > 2).

105 **2.1 Negev Desert FGFs**

Finzi et al. (2020) conducted an extensive survey of fragile geological features (FGF) in the Negev Desert, documenting over 80 FGFs, half of which are rock pillars. For nine rock pillars, the fragility age was determined using the Optical Stimulated Luminescence (OSL) technique, ranging from 123 ky to 1.7 ky. The Negev rock pillars form along pre-existing fracture sets that cut vertically into cliff-forming layers of the hard carbonates of the Judea group. As the fractures grow and widen, they
110 separate rock columns from the cliff (Frayssines and Hantz, 2009;Bakun-Mazor et al., 2013), eventually evolving into freestanding pillars (Fig. 2). The erosional slope retreatment rate in this hyperarid (< 80 mm/y precipitation) area is slow, about 10m Ma^{-1} (Boroda et al., 2014), prevailing since the middle Pleistocene (Enzel et al., 2008). The long-term climatic stability and proximity to seismic sources make the Negev rock pillars excellent candidates for studying their dynamic fragility and testing basic assumptions of regional PSHA.

115 Among the rock pillars mapped in the Negev Desert, the Ramon Pillar (#3001 in Finzi et al., 2020), located at the northern cliff of Ramon crater (30.606N 34.804E), is the most impressive (Fig. 2). The pillar's height is 42 m, with a slenderness ratio

https://doi.org/10.5194/nhess-2024-150
Preprint. Discussion started: 22 August 2024

Natural Hazards and Earth System Sciences
Discussions

(height/width) of 8, comprised mainly of hard carbonates of the upper Cretaceous Hevyon Fm. The fragility age of the pillar, based on OSL dating of silt accumulated in the large crack separating it from the cliff, is 11.4 ky (Finzi et al., 2020).

120

Figure 2. The Ramon pillar: a) photo taken from the Ramon crater floor (left); b) rappelling along the back crack for measurement of rock elastic modulus (right).

3 Methods

3.1 Geometry and Rock Mass Properties

125 The Ramon pillar was scanned using airborne LiDAR (Geoslam ZebHorizon sensor) with a 2 - 4 cm accuracy. A solid model was rendered from the point cloud using the AutoDesk MeshMixer V. 3.5 (https://meshmixer.com/) software bundle.
The density of the Hevyon Fm. hard carbonate is 2,230 kg/m^3, and tensile strength (Brazilian splitting test) ranges from 5 to 9 MPa (Saltzman, 2001). The rock's elastic modulus was estimated from direct measurements of elastic rebound at the back of the Ramon pillar (Fig. 2b). The team led by co-author Tsesarsky rappelled the entire length of the pillar back joint (42 m),
130 taking measurements using a rebound hammer (Proceq Rock Schmidt) at discrete locations along the pillar's height to capture lithological and mechanical variations. The Katz et al. (2000) correlation was applied to estimate the rock elasticity modulus. Rock mass modulus (E_{RM}) was assessed using the Hoek and Diederichs (2006) equation and a GSI value of 65 based on a close visual inspection of the rock mass. The variation of rebound value and E_{RM}, along the height of the pillar, is presented in Fig. 3. Based on these measurements, visual inspection, and geological judgment, we have divided the pillar into four vertical
135 regions, each with a representative rock mass modulus, presented in Fig. 3 as vertical gray lines.

https://doi.org/10.5194/nhess-2024-150
Preprint. Discussion started: 22 August 2024

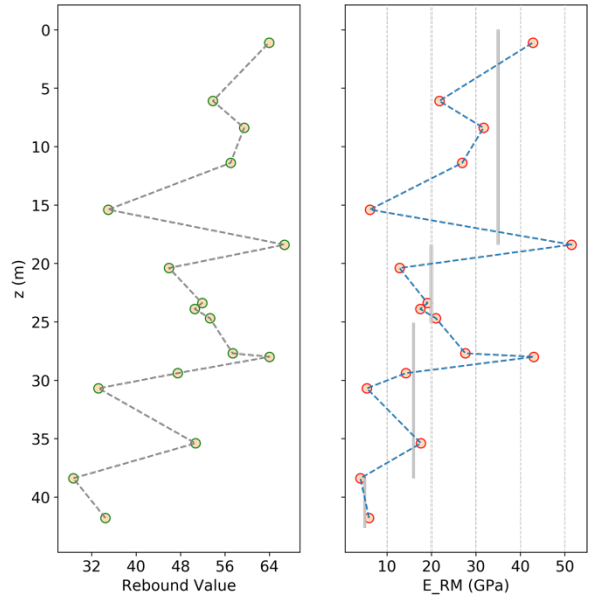

Figure 3. Variation of rock rebound value (left) and rock mass elastic modulus (right) along the Ramon pillar back crack, z is the depth from the surface. Gray lines are representative values for the four vertical regions used in the FE model.

3.2 FEM Analysis

Finite element analysis was performed using the ABAQUS software package (Simulia, 2020). The solid MeshMixer model was imported into ABAQUS and, due to the structure's complex geometry, meshed using tetrahedral linear elements. Convergence analysis was performed to set the optimal element size, resulting in 0.5 m elements. In total, the model comprised $1.248 \cdot 10^6$ elements. For modal analysis, material properties were changed between models from simple homogenous models to models with vertical changes in E_{RM}. Dynamic models were executed using implicit formulation. Loading time histories were selected from the Pacific Earthquake Engineering Research Center (PEER) ground motion database (Ancheta et al., 2013) for selected magnitudes and distances, further elaborated in the Results section.

4 Results

4.1 Modal Analysis

Modal analysis of the pillar with different levels of complexity was performed, starting with an equivalent homogenous cylinder and followed by higher complexity models (refer to Table 1). The "Simplified" model was based on simplified geometry developed from selected cross-sections extracted from photogrammetric scans and interpolated using AutoCAD software. The "Scan_H" and "Scan_M" models were based on high-resolution LiDAR scans, differing in assigned E_{RM}, assumed for the former and measured for the latter. Visualization of the modal analysis for the Scan_M model is presented in

https://doi.org/10.5194/nhess-2024-150
Preprint. Discussion started: 22 August 2024

Natural Hazards and Earth System Sciences
Discussions

Fig. A1. We focus on the first two modes of the pillar (refer to Table 1), as these account for more than 80% of the modal loads (Chopra, 2014).

Table 1. Results of the Ramon Pillar Modal Analysis

Model	E_{RM} (GPa)	Mode 1 (Hz)	Mode 2 (Hz)
Equivalent Cylinder	10	1.4	7.9
	20	2	11.2
Simplified	10	1.76	2.49
	20	2.22	3.14
Scan_H	10	1.5	2.1
	20	2.9	4.22
Scan_M	In-situ	1.3	2.71
Measured		1.32	3.1

These results were compared with measurements of the natural vibration modes reported by Finzi et al. (2020). The original measurements were planned and supervised by co-author Tsesarsky. A broadband seismometer (Geospace GS-1) was positioned on the top of the pillar to record the ambient vibrations. The data were processed using a typical seismic noise data analysis workflow: The instrumental response was removed, and data were detrended and band-pass filtered between 0.1 and 30 Hz (the original recording was performed at 100 Hz). The results of these measurements are presented in Fig. 4 for completeness. The revisited data also contains corrected orientation data.

The first two modes of the pillar are bending modes at 1.32 Hz and 3.1 Hz, clearly visible on the horizontal components. The first mode is bending over the thinner horizontal dimension, normal to the cliff direction (135º), whereas the second mode is bending parallel to the cliff (45º) over the thicker horizontal dimension. The horizontal-to-vertical ratio of the vibrations can be used to define the prominence of the modes, 18 and 13 for the first and second modes, respectively. Higher modes, at 7.5 Hz and 11.1 Hz, are also clearly visible in the two horizontal components. Using the "half power bandwidth" method (Chopra, 2014), the horizontal to vertical channel ratio yields 6% and 4% damping ratios for the 135 and 45 components, respectively.

https://doi.org/10.5194/nhess-2024-150
Preprint. Discussion started: 22 August 2024

Natural Hazards and Earth System Sciences
Discussions

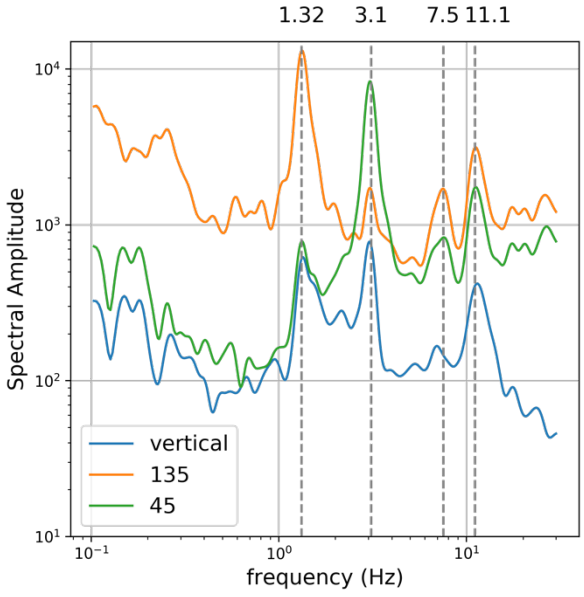

Figure 4. Spectral amplitudes of the Ramon Pillar natural vibrations.

As expected, the calculated modes are determined by the interplay between the rock mass elastic modulus (E_{RM}) value, here changed from 10 GPa to 20 GPa, and the model geometry. Using an equivalent cylinder model shows considerable discrepancy between the measured and calculated modes, specifically in the second mode. Moving forward to a simplified yet more representative geometrical model improves the prediction; however, it still has low accuracy. The two scanned models exemplify the difference between assumed and measured E_{RM}. For the "Scan_H" model, assuming E_{RM} = 10 GPa yields a good approximation of the first vibration mode: 1.5 Hz compared with measured 1.32 Hz. However, the second vibration mode is considerably lower than measured, 2.1 Hz compared with 3.1 Hz. Assuming E_{RM} = 20 GPa increases the discrepancy in both modes. Using the same geometry, however, with in-situ determined E_{RM}, including vertical variations, yields the most accurate results. The first vibration mode is 1.3 Hz, measured and calculated, and the second mode is 3.1 Hz measured compared to 2.7 Hz calculated. The discrepancy between the measured and modeled in the second mode suggests that the model could be further refined, specifically the vertical distribution elastic modulus. We consider the accurate predictions of the natural vibration modes to be the validation of our FE model for the Ramon pillar and use this model for dynamic analysis.

4.2 Simplified Fragility Analysis

Before performing a FEM dynamic analysis, with its computational demands, we studied the pillar's fragility using the following simplified approach. We defined a maximum magnitude earthquake for each causative fault with the closest distance to the Ramon Pillar, refer to Table 2. The pseudo-spectral accelerations (PSA) for each scenario were calculated using the ASK14 ground motion model (Abrahamson et al., 2014). Figure A2 in Appendices presents the PSA of the different scenarios. Assuming that the pillar behaves as a cantilever, which was proven by the in-situ measurements and modeling, we calculated

https://doi.org/10.5194/nhess-2024-150
Preprint. Discussion started: 22 August 2024

Natural Hazards and Earth System Sciences Discussions

the moment and the tensile stresses at the base of the cantilever, assuming an equivalent cylinder with R = 3.8 m. For the calculation, we used an elastic modulus of 13 GPa, which gave the best compliance with the first natural mode of 1.32 Hz. We used the median and one standard deviation value for each scenario. The results of the analysis are presented in Table 2.

For each of the scenarios studied, the median tensile stress at the base of the pillar is below the tensile strength of the rock. The highest value is 2.5 MPa for the Ramon fault scenario, and the lowest value is for the Paran fault scenario, 1 MPa. These values are lower than the tensile strength of the rock (5 – 9 MPa). Assuming a 50% strength reduction due to incipient discontinuities will bring the tensile stresses at the base to the lower bound of rock strength only for the Ramon fault scenario. Taking into account one standard deviation (1SD) the stresses at the base of the pillar are typically doubled. For the Ramon scenario, the tensile stress is 4.6 MPa, and for the Nafha-Saad and Arava scenarios, it is 3.8 MPa, bringing the stresses at the base of the pillar close to failure.

Table 2. Results of the Simplified Fragility Analysis for an equivalent cylinder (R = 3.8m). PGA is peak ground acceleration; values in parentheses are plus one standard deviation. SA @f_1 is the median spectral acceleration at the first natural mode, SD is the standard deviation, and σ_t is the median tensile stress at the base of the pillar. PGA and SA were calculated using the ASK14 ground motion model.

Scenario	Causative fault	PGA (g)	SA @f_1 (g)	SA @f_1 + SD (g)	σ_t (MPa)	σ_t +SD (MPa)
M 6 R 6	Ramon	0.21 (0.40)	0.13	0.26	2.5	4.6
M 6.2 R 10	Nafha-Saad	0.15 (0.30)	0.09	0.18	1.9	3.8
M 6.2 R 26	Paran	0.06 (0.12)	0.04	0.08	1	1.8
M 7.5 R 45	Arava	0.08 (0.15)	0.08	0.17	1.8	3.6

4.3 Dynamic Analysis

The dynamic analysis focuses on loading scenarios typical to the seismic sources of the region: M 6.2 on the SNSZ faults and M 7 on the DST. For the SNSZ, we focused on R_{RUP} < 10 km, representing earthquakes on the Ramon and Saad-Nafha faults. For the DST, we assume an R_{RUP} of 45 km, the shortest distance to the Arava fault. Event names and ground motion parameters are presented in Table 3. For each event, the two horizontally perpendicular loading components were simulated.

The first step of our analysis was to study the effect of damping on the pillar's stresses and displacements. Damping ratios for freestanding rock structures depend on geometry, mass and stiffness distribution, degree of continuity, and other attributes of natural rock masses. Finnegan et al. (2022), and references therein show that for sandstone freestanding rock structures, the damping ratio ranges from ~ 1% to 3%; however, higher values of ~ 8% to 10% have been reported for jointed rock masses.

https://doi.org/10.5194/nhess-2024-150
Preprint. Discussion started: 22 August 2024


Natural Hazards and Earth System Sciences Discussions

Our estiemate for the Ramon pillar fall within the reported range, with a damping ratio of about 5%. In Abaqus, we used a Rayleigh damping of 2%, 5%, and 7% to study the variations of the tensile stress at the pillar's base and the displacement at the top. For this part, we used the Morgan Hill M 6.2 earthquake (refer to Table 2). As expected, the maximal tensile stress and the displacements diminished with damping. The tensile stresses reduced from 15.6 MPa for 2% to 10.3 MPa for 5% and 8.65 MPa for 7% damping. Respectively, the displacement at the top of the pillar reduced from 0.07 m to 0.04 m and 0.037 m. The sensitivity to the damping ratio is maximal when changing the value from 2% to 5%, the tensile stress value changes by 34%, and the displacement by 57%. Further increasing the damping ratio results in considerably lesser changes. Based on the measurements and the sensitivity study results, we have decided to proceed with 5% damping in our dynamic analysis.

A typical result of the dynamic analysis is presented in Fig. 5. Please note that each component is loaded in one direction at a time, representing the thinner and thicker dimensions of the pillar, respectively. H1 is loaded in the 135° direction and H2 in the 45° direction. Each loading component results in different stresses at the base and displacements at the top of the pillar, reflecting both the loading time history (amplitude and duration) and the direction of loading. The main difference between the two loading histories arises from the amplitude of the surface waves. In the H1 direction, the amplitude of the surface waves is considerably lower than the amplitude of the shear waves, whereas, in the H2 direction, the surface wave amplitude is in the same order as the amplitude of the shear waves. The strong later "jolt" of the surface waves in the H2 direction results in a 30% increase of the tensile stresses at the pillar's base, from 10.4 MPa to 13.3 MPa. The results of the other earthquakes analyzed are presented in Table 4.

The highest tensile stress value at the pillar's base is 17.68 MPa for the Chi-Chi M 6.2 H1 component. The lowest tensile stress value at the pillar's base is 5.85 MPa for the Parkfield M 6 (R_{RUP} = 10 km) H1 component. It should be noted that these two extremes reflect the different faulting styles between the two events; whereas the Chi-Chi event (an aftershock of the M_w 7.7 event) is reverse faulting, the Parkfield event is a strike-slip. Typically, reverse faults produce stronger ground motions than strike-slip faults (such as SNSZ or DST). However, we wanted to study the dynamic behavior of the pillar under various loading scenarios with different PGA, IA, and duration. The scenario of a remote M 7 earthquake, represented by the 1999 Duzce M 7.2 event, results in relatively low tensile stress and displacement: 3.92 MPa and 0.003 m, respectively.

https://doi.org/10.5194/nhess-2024-150
Preprint. Discussion started: 22 August 2024

Natural Hazards and Earth System Sciences
Discussions

240 **Table 3. Earthquakes catalog used in the dynamic analysis of the Ramon Pillar. M is the magnitude, R_{RUP} is the distance to rapture, PA is the peak acceleration, IA is the Arias intensity, and t_{595} is the significant duration of the event. H1 and H2 are the horizontal components. Ground motion time histories were downloaded from the PEER strong motion database (Ancheta et al., 2013).**

Event	Mw	R_{rup} (km)	PA H1 (g)	IA H1 (m/sec)	t_{595} H1 (sec)	PA H2 (g)	IA H2 (m/sec)	t_{595} H2 (sec)
Morgan Hill 1984	6.2	10	0.22	0.4	7.30	0.29	0.8	6.5
Parkfield 2004 (a)	6	10	0.15	0.15	9.95	0.17	0.17	11.04
Parkfield 2004 (b)	6	6	0.79	1.2	3.19	0.43	0.42	6.9
Chi-Chi 1999	6.3	6	0.34	1.5	5.81	0.32	1.3	7.33
Duzce 1999	7.2	45	0.03	0.008	23.20	0.02	0.005	26.3

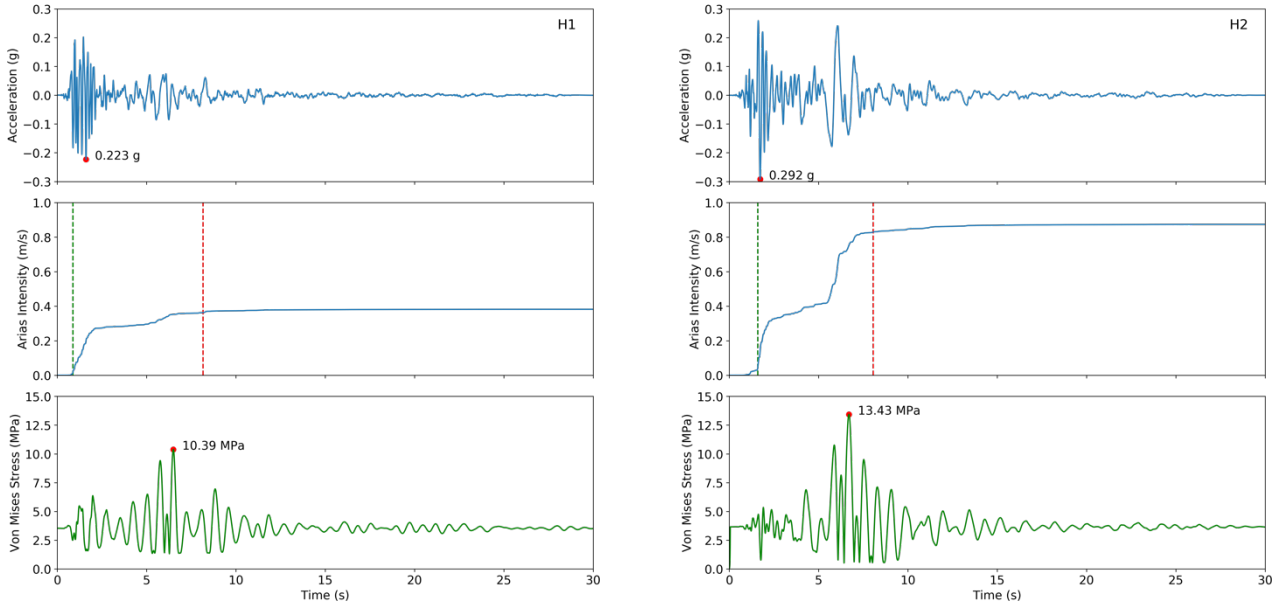

245 **Figure 5. Results of the Ramon Pillar dynamic analysis for the Morgan Hill 1984 earthquake with M 6 and R_{RUP} = 10 km. The left panel is the H1 loading component, and the right panel is the H2 loading component. From the top: acceleration time history, Arias Intensity(vertical lines are t5 and t95 values), and maximal tensile (Von Mises) stress at the bottom of the pillar.**

https://doi.org/10.5194/nhess-2024-150
Preprint. Discussion started: 22 August 2024

Natural Hazards and Earth System Sciences Discussions

Table 4. Horizontal displacement (δh) at the top of the pillar and tensile stress (σ_t) at the bottom of the pillar for the ground motions modeled. H1 and H2 are the horizontal components of ground motion.

Event	M	R_{rup} (km)	σ_t H1 (MPa)	δ_T H1 (m)	σ_t H2 (MPa)	δ_T H2 (m)
Morgan Hill 1984	6.2	10	10.39	0.044	13.43	0.039
Parkfield 2004 (a)	6	10	6.02	0.023	5.85	0.012
Parkfield 2004 (b)	6	6	7.88	0.035	5.87	0.012
Chi-Chi 1999	6.3	6	17.86	0.085	14.30	0.04
Duzce 1999	7.2	45	4.18	0.01	3.92	0.003

5 Discussion

PBR stability analysis implicitly assumes that a hard, discontinuous contact (no moments resistance) exists between the base and the pedestal. In sedimentary rock masses, such as the Cretaceous carbonates of the Northern Negev, this assumption is not satisfied as many discontinuities, and beddings specifically, contain rock bridges with considerable tensile strength. Our measurements of natural vibrations of the Ramon pillar and subsequent FE modal analysis show that the pillar behaves as a cantilever. Static FEM analysis pillar shows that due to eccentric geometry and irregular geometry, the maximum tensile stress at the base of the pillar is 3.6 MPa. This value can be regarded as the lower bound of basal strength, including incipient discontinuities and rock bridges. Compared with the rock tensile strength, 5 to 9 MPa, this value represents a 56% to 20% strength reduction of the laboratory strength.

A simplified analysis based on an equivalent cylinder model and loads based on the ASK14 GMM shows that for the scenarios studied, only the Ramon fault (M 6 and R_{Rup} = 6 km) can induce tensile stresses high enough to overcome the basal strength (refer to Fig. 6). For the median load, the basal tensile stress, 2.6 MPa, is well below the strength, and only for the single standard deviation load, the tensile stress is 4.6 MPa, which is higher by 20% only than the basal strength. Other scenarios yielded stresses lower than basal strength.

Assuming that the basal strength was exceeded for the Ramon fault scenario and that the pillar is entirely disconnected requires a renewed analysis of the pillar in terms of PBR. Finzi et al. (2020) report a critical acceleration of 0.12g and dynamic acceleration (Anooshehpoor et al., 2004) of 0.16g for the toppling of the Ramon pillar, assuming entirely discontinuous basal conditions. For the Ramon scenario, the median PGA of 0.21 g is larger than the dynamic value, and for the Nafha-Saad scenario, it is slightly lower. For the Paran and Arava scenarios, median PGA values, 0.06 and 0.08 g, respectively, are considerably lower than the dynamic acceleration value. The 1SD PGAs are larger than the dynamic acceleration, rendering

https://doi.org/10.5194/nhess-2024-150
Preprint. Discussion started: 22 August 2024

Natural Hazards and Earth System Sciences
Discussions

the Ramon and Nafha-Saad scenarios unstable. However, the Paran and Arava scenario's PGAs are still lower than the dynamic acceleration required to topple the pillar.

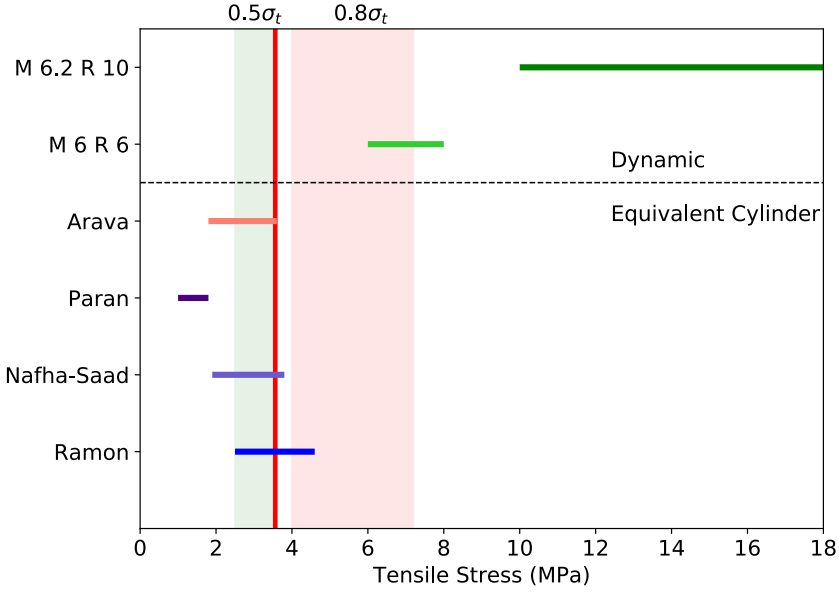

Figure 6. Compilation of basal stresses for the Ramon Pillar analysis. For the Equivalent Cylinder models, the horizontal bar spans the tensile stresses for the spectral acceleration's median (low) and single standard deviation (high) at 1.32 Hz. For the Dynamic analysis, the horizontal bar spans the minimum and maximum tensile stresses. The vertical line at 3.6 MPa represents the maximum static basal stress. Shaded regions span the 80% (pink) and 50% (green) range of laboratory rock tensile strength.

5.1 Dynamic Fragility

The equivalent cylinder analysis is based on a time-invariant, single-value (PSA) determination of basal stresses. However, dynamic loading is time-dependent. To this end, we performed a fully dynamic analysis using the validated FE model. The selected time series represent a range of acceleration and duration values (Table 3), from 0.15 to 0.75 g and 3 sec to 10 sec. Naturally, the modeled ground motions do not encompass a full suite of accelerations and durations but show general trends. Clearly, the dynamic analysis results in higher basal stresses. The minimal increase in tensile stresses was calculated for the Parkfield 2004 event (PGA of ~0.2g and IA of ~0.2 m/sec with duration of ~ 10 sec) to a value of 6 MPa, a factor of two higher than the static basal strength. The Morgan Hill 1984 event (PGA of ~0.3g and IA of ~0.4 to 0.8 m/sec with a duration of ~ 7 sec) increased the tensile stresses to 10 MPa and 13 MPa. The highest stresses were calculated for the M 6.2 Chi-Chi 1999 (an aftershock of the M_w 7.7 event) with 14 MPa and 18 MPa values in the two horizontal components. Interestingly, the pulse-like loading of the Parkfield (b) event at R_{Rup} = 6 km, with a PGA of 0.7 g and a duration of 3 sec, yielded similar displacement and stress values to the Parkfield (a) event (PGA = 0.17 g and duration of 11 sec) showing the detrimental effect of lower PGA with higher duration. Loading the pillar by a larger yet distant earthquake, represented by the

https://doi.org/10.5194/nhess-2024-150
Preprint. Discussion started: 22 August 2024


Natural Hazards and Earth System Sciences Discussions

M 7.2 Duzce 1999 earthquake, at R_{RUP} = 45 km (not shown in Fig. 6), bares little effect on the pillar, elevating the stresses by only 17% and 9% for the two horizontal components above the static values.

In this research, we modeled the pillar as a continuous cantilever structure fixed at its bottom. The accurate forward calculation of the natural vibration modes performed in this research supports the validity of our model and modeling approach. The rock mass's discontinuous nature was incorporated in the GSI rating for calculating rock mass modulus. Under this assumption, the stresses at the pillar's base are maximal, as no frictional sliding or rocking is allowed, and the only energy dissipation is through the viscous Rayleigh damping. We used a value of 5%, which is similar to the measured damping. Modeling sliding and rocking in FE is challenging as incorporating discontinuities into the continuous model is not trivial. An alternative approach is utilizing Discrete Element Methods (DEM) to study dynamic fragility. However, numerous numerical controls, such as penalties and frictional properties, are not easily calibrated or measured in situ. Furthermore, assessing the amount and distribution of rock bridges across bedding and joints is a non-trivial task. It should be recalled that even 5% of rock bridges stabilize cliffs of carbonate rocks (Elmo et al., 2018).

5.1 Implications for Seismic Hazard

The Ramon pillar is not sensitive to loading from strong and remote earthquakes (M 7 and R_{RUP} > 45 km) and, therefore, cannot be used to constrain the seismic hazard from the DST. However, it was found to be sensitive to moderate and close earthquakes (M 6 and R_{RUP} < 10 km) originating on the SNSZ. The equivalent cylinder approach and GMM-based load results in a non-conservative estimate of basal stresses. Fully dynamic analysis yields considerably higher stresses and indicates that the Ramon Pillar is sensitive to close earthquakes.

All of the M 6 earthquakes modeled dynamically induce tensile stresses at the pillar's base that are higher than its basal strength. The first exceedance of the strength typically occurs in the first seconds of the loading, typically within 25% of the loading duration (t_{595}), well before reaching the peak stress. Thus, it can be assumed that a bedding plane with rock bridges will fail during loading, leading to detachment of the base. Under fully discontinuous conditions and assuming rocking mechanics (PBR type), the required dynamic acceleration to topple the pillar is 0.16g, well within the PGA range for the magnitude-distance of the SNSZ faults.

Based on the presented analysis, we postulate that an M 6 event on the Ramon and Nafha-Sa'ad faults didn't occur during the pillar's fragility age, over the past 11,000 years. Our analysis challenges the assumption that the SNSZ as a whole can produce an M 6.2 earthquake. To determine whether the southern Paran fault is capable of an M 6.2 earthquake, a closer FGF should be analyzed.

The analysis presented here is the first step to constrain the seismic hazard on the SNSZ, and more FGFs in the region should be analyzed for better temporal and spatial coverage. The work of Finzi et al. (2020) lists nine pillars in this region (including the Ramon pillar) with fragility ages ranging from 1.4 ky to 123 ky. It should be recalled here that typically, the number of FGFs used for constraining PSHA is low; please refer to recent examples of Rood et al. (2024) and Stirling et al. (2021).

https://doi.org/10.5194/nhess-2024-150
Preprint. Discussion started: 22 August 2024


Natural Hazards and Earth System Sciences
Discussions

6 Conclusions

This research studied the dynamic fragility of a 42 m high, slender rock column comprised of discontinuous sedimentary rock mass located on the rim of the Ramon erosional crater (Israel). The pillar is found near two seismic sources: The Sinai Negev shear zone (SNSZ) and the Dead Sea transform (DST).

The pillar was aerially scanned with high-precision LiDAR. Rock mass elastic stiffness was measured in situ by rappelling the entire length of the pillar. Based on the scan and measurements, a finite element (FE) model for the pillar was developed.

The FE model was validated by comparing the modal analysis (assuming cantilever boundary conditions) results to the in-situ measured vibrational modes of the pillar. The comparison shows that the first two modes are highly compatible: 1.3 Hz and 3 Hz measured vs. 1.3 Hz and 2.7 Hz modeled.

We first studied the pillar's fragility using a simplified approach based on pseudo-spectral accelerations and an equivalent cylinder with R = 3.8 m. For the different scenarios studied, only the M 6 and R_{RUP} = 6 km scenario yielded basal stresses exceeding the pillar's basal strength, while other scenarios resulted in considerably lower stresses.

A fully dynamic fragility analysis was performed based on the favorable validation of the FE model. Two major scenarios were studied: M 6 earthquake with R_{Rup} < 10 km on one of the potentially active faults of the Sinai Negev Shear Zone, and M 7 earthquake with R_{Rup} = 45 km on the active Dead Sea Transform. For the M 6 earthquakes, the dynamic analysis yielded considerably higher basal stresses than the equivalent cylinder analysis. The dynamic stresses exceed the basal strength of the pillar, y a factor of two or higher.

Based on our findings, we postulate that the M 6 scenario on the SNSZ should lead to breakage of the Ramon pillar at its base due to tensile stresses exceeding its strength. Conservatively assuming that the first exceedance does not lead to pillar collapse, but does change the mechanical behavior from cantilever to PBR, it predicts a toppling failure during the next M 6 earthquake. With a fragility age of 11.4 ky, our analysis challenges the assumption that the SNSZ as a whole can produce an M 6 event.

https://doi.org/10.5194/nhess-2024-150
Preprint. Discussion started: 22 August 2024

Natural Hazards and Earth System Sciences
Discussions
Open Access
EGU

Appendices

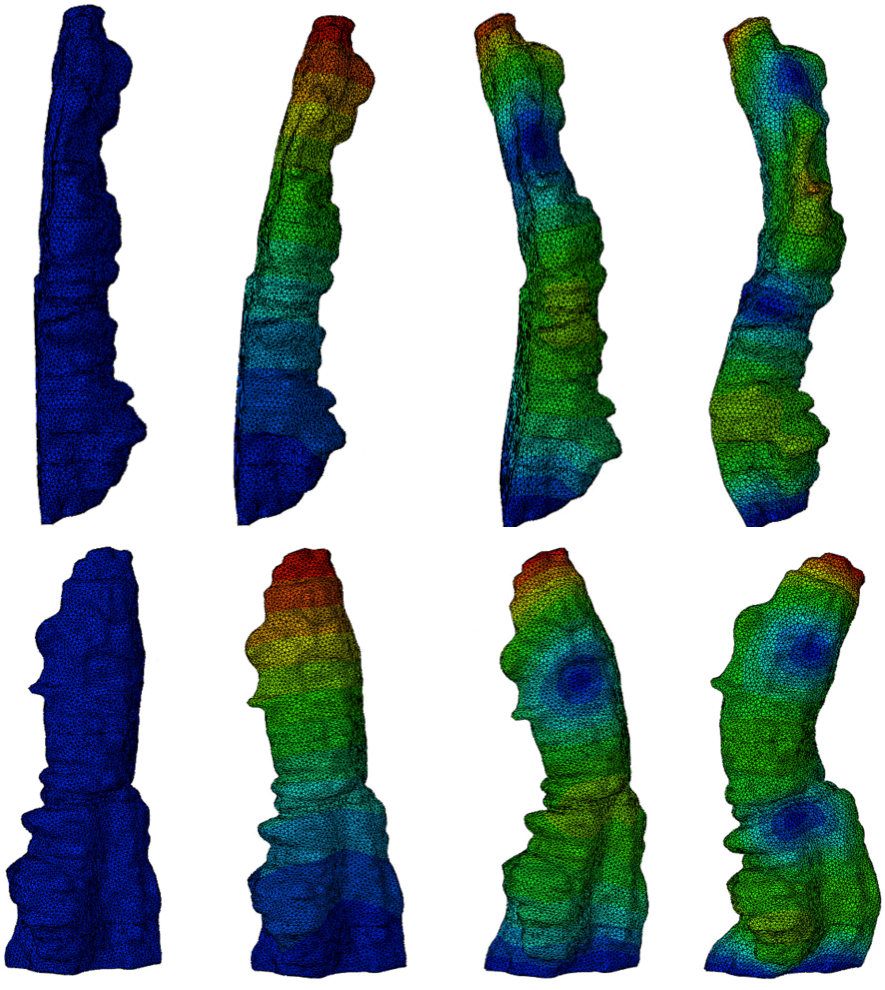

Figure A1. Modal analysis visualization of the Scan_H model. Top: 145º direction and bottom 35º direction.

https://doi.org/10.5194/nhess-2024-150
Preprint. Discussion started: 22 August 2024

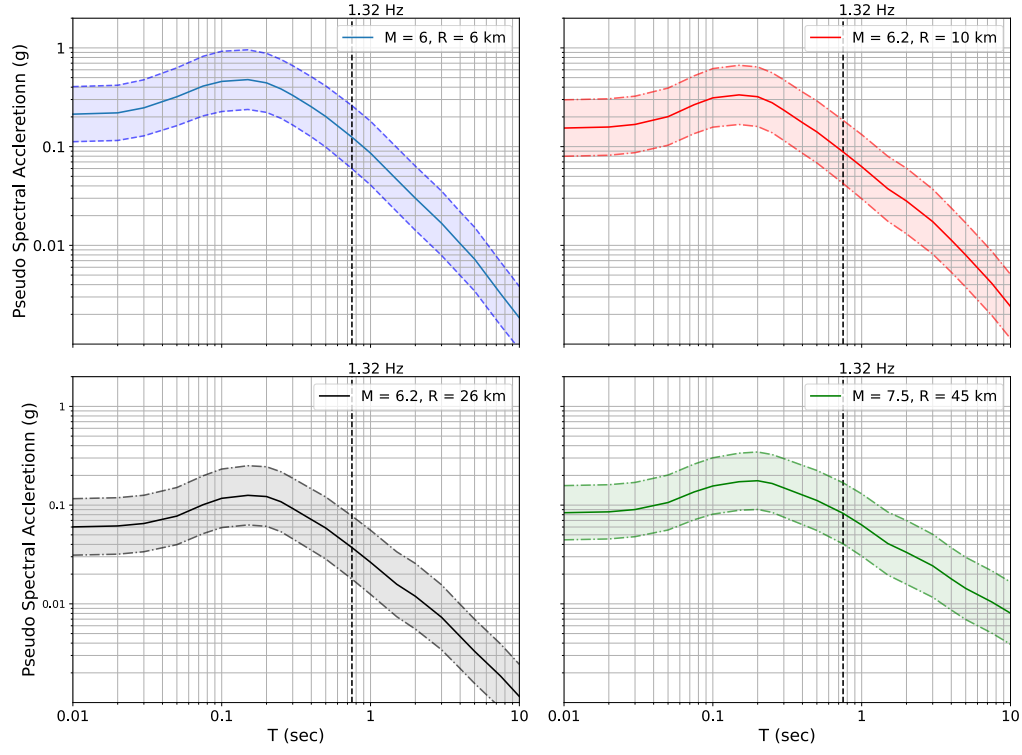

Figure A2. Pseudo-spectral accelerations for the different fault–distance scenarios based on the ASK14 (Abrahamson et al., 2014) ground motion model. The continuous line is the median value; broken lines are one standard deviation. 1.32 Hz is the first mode of the Ramon pillar.

Data Availability

Data will be made available on request.

Authorship contribution statement

A. Jbara: Investigation, Formal analysis, Writing. M. Tsesarsky: Conceptualization, Funding acquisition, Supervision, Methodology, Investigation, Writing.

Declaration of competing interest

The authors declare that they have no known competing interests that could have influenced the work reported in this paper.

https://doi.org/10.5194/nhess-2024-150
Preprint. Discussion started: 22 August 2024

Natural Hazards and Earth System Sciences Discussions

Acknowledgments

This research was partially sponsored by the Israel Science Foundation, grant 1163/22. We thank Boaz Langford for his assistance with rappeleing and in-situ measurments.

References

Abrahamson, N. A., Silva, W. J., and Kamai, R.: Summary of the ASK14 Ground Motion Relation for Active Crustal Regions, Earthquake Spectra, 30, 1025-1055, 10.1193/070913eqs198m, 2014.

Agnon, A.: Pre-Instrumental Earthquakes Along the Dead Sea Rift, in: Dead Sea Transform Fault System: Reviews, edited by: Garfunkel, Z., Ben-Avraham, Z., and Kagan, E., Springer, 207-262, 2014.

Ambraseys, **N.**, Melville, C. P., and Adams, R. D.: The seismicity of Egypt, Arabia and the Red Sea: a historical review, Cambridge UniversityPress, 180 pp., 2005.

Ancheta, T. D., Darragh, R. B., Stewart, J. P., Seyhan, E., Silva, W. J., Chiou, B. S. J., Wooddell, K. E., Graves, R. W., Kottke, A. R., Boore, D. M., Kishida, T., and Donahue, J. L.: PEER NGA-West2 Database Pacific Earthquake Engineering Research center2013/03, 2013.

Anderson, J. G., Brune, J. N., Biasi, G., Anooshehpoor, A., and Purvance, M.: Workshop Report: Applications of Precarious Rocks and Related Fragile Geological Features to U.S. National Hazard Maps, Seismological Research Letters, 82, 431-441, 10.1785/gssrl.82.3.431, 2011.

Anooshehpoor, A., Brune, J. N., and Zeng, Y.: Methodology for Obtaining Constraints on Ground Motion from Precariously Balanced Rocks, Bulletin of the Seismological Society of America, 94, 285-303, 10.1785/0120020242, 2004.

Bakun-Mazor, D., Hatzor, Y. H., Glaser, S. D., and Carlos Santamarina, J.: Thermally vs. seismically induced block displacements in Masada rock slopes, International Journal of Rock Mechanics and Mining Sciences, 61, 196-211, https://doi.org/10.1016/j.ijrmms.2013.03.005, 2013.

Bommer, J. J.: Earthquake hazard and risk analysis for natural and induced seismicity: towards objective assessments in the face of uncertainty, Bulletin of Earthquake Engineering, 20, 2825-3069, 10.1007/s10518-022-01357-4, 2022.

Boroda, R., Matmon, A., Amit, R., Haviv, I., Arnold, M., Aumaître, G., Bourlès, D. L., Keddadouche, K., Eyal, Y., and Enzel, Y.: Evolution and degradation of flat-top mesas in the hyper-arid Negev, Israel revealed from 10Be cosmogenic nuclides, Earth Surface Processes and Landforms, 39, 1611-1621, https://doi.org/10.1002/esp.3551, 2014.

Brune, J. N.: Precariously balanced rocks and ground-motion maps for Southern California, Bulletin of the Seismological Society of America, 86, 43-54, 1996.

Chopra, A. K.: Dynamics of Structures, 4th ed., Pearson, 944 pp., 2014.

Elmo, D., Donati, D., and Stead, D.: Challenges in the characterisation of intact rock bridges in rock slopes, Engineering Geology, 245, 81-96, https://doi.org/10.1016/j.enggeo.2018.06.014, 2018.

https://doi.org/10.5194/nhess-2024-150
Preprint. Discussion started: 22 August 2024

Enzel, Y., Amit, R., Dayan, U., Crouvi, O., Kahana, R., Ziv, B., and Sharon, D.: The climatic and physiographic controls of the eastern Mediterranean over the late Pleistocene climates in the southern Levant and its neighboring deserts, Global and Planetary Change, 60, 165-192, https://doi.org/10.1016/j.gloplacha.2007.02.003, 2008.

Finnegan, R., Moore, J. R., Geimer, P. R., Dzubay, A., Bessette-Kirton, E. K., Bodtker, J., and Vollinger, K.: Ambient Vibration Modal Analysis of Natural Rock Towers and Fins, Seismological Research Letters, 93, 1777-1786, 10.1785/0220210325, 2022.

Finzi, Y., Ganz, N., Dor, O., Davis, M., Volk, O., Langer, S., Arrowsmith, R., and Tsesarsky, M.: Stability Analysis of Fragile Rock Pillars and Insights on Fault Activity in the Negev, Israel, Journal of Geophysical Research: Solid Earth, 125, e2019JB019269, https://doi.org/10.1029/2019JB019269, 2020.

Frayssines, M., and Hantz, D.: Modelling and back-analysing failures in steep limestone cliffs, International Journal of Rock Mechanics and Mining Sciences, 46, 1115-1123, https://doi.org/10.1016/j.ijrmms.2009.06.003, 2009.

Garfunkel, Z.: Lateral motion and deformation along the Dead Sea transform, in: Dead Sea Transform Fault System: Reviews, edited by: Garfunkel, Z., Ben-Avraham, Z., and Kagan, E. J., Springer, Dordrecht, the Netherlands, , 109–150, 2014.

Gerstenberger, M. C., Marzocchi, W., Allen, T., Pagani, M., Adams, J., Danciu, L., Field, E. H., Fujiwara, H., Luco, N., Ma, K.-F., Meletti, C., and Petersen, M. D.: Probabilistic Seismic Hazard Analysis at Regional and National Scales: State of the Art and Future Challenges, Reviews of Geophysics, 58, e2019RG000653, 10.1029/2019rg000653, 2020.

Grünthal, G., Hakimhashemi, A., Schelle, H., Bosse, C., and Wahlström, R.: The long-term temporal behaviour of the seismicity of the Dead Sea Fault Zone and its implication for time-dependent seismic hazard assessments., GFZ, Potsdam, 48, 2009.

Hamiel, Y., Piatibratova, O., and Mizrahi, Y.: Creep along the northern Jordan Valley section of the Dead Sea Fault, Geophysical Research Letters, 43, 2494-2501, doi:10.1002/2016GL067913, 2016.

Hoek, E., and Diederichs, M. S.: Empirical estimation of rock mass modulus, International Journal of Rock Mechanics and Mining Sciences, 43, 203-215, DOI 10.1016/j.jijrmms.2005.06.005, 2006.

Katz, O., Reches, Z., and Roegiers, J. C.: Evaluation of mechanical rock properties using a Schmidt Hammer, International Journal of Rock Mechanics and Mining Sciences, 37, 723-728, https://doi.org/10.1016/S1365-1609(00)00004-6, 2000.

Klinger, Y., Le Beon, M., and Al-Qaryouti, M.: 5000 yr of paleoseismicity along the southern Dead Sea fault, Geophysical Journal International, 202, 313-327, 10.1093/gji/ggv134, 2015.

Lefevre, M., Klinger, Y., Al-Qaryouti, M., Le Béon, M., and Moumani, K.: Slip deficit and temporal clustering along the Dead Sea fault from paleoseismological investigations, Scientific Reports, 8, 4511, 10.1038/s41598-018-22627-9, 2018.

Marzocchi, W., and Meletti, C.: PSHA: Does It Deal with What It Is or What We Want It to Be?, Seismological Research Letters, 10.1785/0220230418, 2024.

Moore, J. R., Thorne, M. S., Koper, K. D., Wood, J. R., Goddard, K., Burlacu, R., Doyle, S., Stanfield, E., and White, B.: Anthropogenic sources stimulate resonance of a natural rock bridge, Geophysical Research Letters, 43, 9669-9676, 10.1002/2016gl070088, 2016.

https://doi.org/10.5194/nhess-2024-150
Preprint. Discussion started: 22 August 2024

Moore, J. R., Geimer, P. R., Finnegan, R., and Thorne, M. S.: Use of Seismic Resonance Measurements to Determine the Elastic Modulus of Freestanding Rock Masses, Rock Mechanics and Rock Engineering, 51, 3937-3944, 10.1007/s00603-018-1554-6, 2018.

Moore, J. R., Geimer, P. R., Finnegan, R., and Michel, C.: Dynamic Analysis of a Large Freestanding Rock Tower (Castleton Tower, Utah), Bulletin of the Seismological Society of America, 109, 2125-2131, 10.1785/0120190118, 2019.

Mulargia, F., Stark, P. B., and Geller, R. J.: Why is Probabilistic Seismic Hazard Analysis (PSHA) still used?, Physics of the Earth and Planetary Interiors, 264, 63-75, https://doi.org/10.1016/j.pepi.2016.12.002, 2017.

Rood, A. H., Rood, D. H., Stirling, M. W., Madugo, C. M., Abrahamson, N. A., Wilcken, K. M., Gonzalez, T., Kottke, A., Whittaker, A. C., Page, W. D., and Stafford, P. J.: Earthquake Hazard Uncertainties Improved Using Precariously Balanced Rocks, AGU Advances, 1, e2020AV000182, 10.1029/2020av000182, 2020.

Rood, A. H., Stafford, P. J., and Rood, D. H.: San Andreas Fault Earthquake Hazard Model Validation Using Probabilistic Analysis of Precariously Balanced Rocks and Bayesian Updating, Seismological Research Letters, 95, 1776-1793, 10.1785/0220220287, 2024.

Saltzman, B.: Possible correlation between the mechanical layer's joint spacing and rock mechanical properties. , M.Sc. thesis. Ben Gurion University of the Negev, 2001.

Shamir, G., Bartov, Y., Sneh, A., Fleischer, L., Arad, V., and Rosensaft, M.: Preliminary seismic zonation for Israel. GII Report No. 550/95/01(1), 2001.

Shang, J., West, L. J., Hencher, S. R., and Zhao, Z.: Tensile strength of large-scale incipient rock joints: a laboratory investigation, Acta Geotechnica, 13, 869-886, 10.1007/s11440-017-0620-7, 2018.

Simulia: Abaqus Users' Manual. Dassault Systèmes Simulia Corporation, 2020.

Stark, P. B.: Pay No Attention to the Model Behind the Curtain, Pure Appl. Geophys., 179, 4121-4145, 10.1007/s00024-022-03137-2, 2022.

Stirling, M. W., and Anooshehpoor, R.: Constraints on Probabilistic Seismic-Hazard Models from Unstable Landform Features in New Zealand, Bulletin of the Seismological Society of America, 96, 404-414, 10.1785/0120050034, 2006.

Stirling, M. W., Oskin, M. E., Arrowsmith, J. R., Rood, A. H., Goulet, C. A., Grant Ludwig, L., King, T. R., Kottke, A., Lozos, J. C., Madugo, C. M., McPhillips, D., Rood, D. H., Sleep, N. H., and Wittich, C. E.: Evaluation of Seismic Hazard Models with Fragile Geologic Features, Seismological Research Letters, 10.1785/0220200197, 2020.

Stirling, M. W., Abbott, E. R., Rood, D. H., McVerry, G. H., Abrahamson, N. A., Barrell, D. J. A., Huso, R., Litchfield, N. J., Luna, L., Rhoades, D. A., Silvester, P., Van Dissen, R. J., Van Houtte, C., and Zondervan, A.: First Use of Fragile Geologic Features to Set the Design Motions for a Major Existing Engineered Structure, Bulletin of the Seismological Society of America, 111, 2673-2695, 10.1785/0120210026, 2021.

Valentin, J., Capron, A., Jongmans, D., Baillet, L., Bottelin, P., Donze, F., Larose, E., and Mangeney, A.: The dynamic response of prone-to-fall columns to ambient vibrations: comparison between measurements and numerical modeling, Geophysical Journal International, 208, 1058-1076, 10.1093/gji/ggw440, 2017.

Zohar, M.: Temporal and Spatial Patterns of Seismic Activity Associated with the Dead Sea Transform (DST) during the Past 3000 Yr, Seismological Research Letters, 10.1785/0220190124, 2019.